

Model Uncertainties of the 2002 Update of California Seismic Hazard Maps

Award Number 04HQGR0027

Principal Investigator: Tianqing Cao
California Geological Survey, Sacramento, CA 95814

Abstract

In this paper we present uncertainty and sensitivity estimates for the 2002 update of the California probabilistic seismic hazard maps to explore the model uncertainty and parametric sensitivity. Our analysis implements a Monte Carlo simulation approach that allows for independent sampling from fault to fault in each simulation. This sampling yields lower uncertainties than dependent sampling that has been used in some other published uncertainty analysis. The uncertainty maps of the seismic hazards are explained by the fundamental uncertainty patterns from four basic test cases, in which the uncertainties from one-fault and two-fault systems are studied in detail. For a fault having moderate magnitude ($M \sim 7$) earthquakes, the coefficient of variation (standard deviation divided by mean, COV) of ground motion decreases with increasing distance from the fault and then increases. This is primarily due to the fact that the attenuation relations disagree with each other less at distances around 40 to 50 km. For a fault having large magnitude ($M \sim 7.5$) earthquakes, the COV decreases with increasing distance from the fault and then levels off at about 30 to 40 km. For such a fault, the dominant contribution to uncertainty is the difference between characteristic and Gutenberg-Richter modeling of seismic recurrence. This modeling difference does not have a minimum value at certain characteristic distance like the attenuation relations. The two-fault system shows a decrease in COV where more than one fault or fault segment are close to each other and these faults jointly bring the COV values to lower than from one fault alone.

The COV map of peak ground accelerations (10% of exceedance in 50 years) for California shows lower values (0.1 to 0.15) along the San Andreas fault system and other class A faults than along those class B faults (0.2 to 0.3). This is mostly because the former are modeled pure characteristic and the latter characteristic and Gutenberg-Richter. The COV values decrease with increasing distance from the San Andreas fault system and then increase due to mostly the uncertainties of attenuation relations. High COV values (0.4 to 0.6) are found around the Garlock, Anacapa-Dume, and Palos Verdes faults in southern California and around the Maacama fault and Cascadia subduction zone in northern California. It is mostly due to the characteristic vs. Gutenberg-Richter modeling, the magnitude uncertainty, and the relative isolation of these faults or no adjacent faults to jointly bring the COV down. The samples of decreased COV values owing to adjacent faults can be found around the places where Garlock fault and Mojave and Carrizo segments are close to each other and where San Jacinto fault and Mojave and San Bernardino segments are close to each other.

Introduction

The California Geological Survey (CGS) joined the U.S. Geological Survey (USGS) in an extensive effort to update the 1996 California portion of the national seismic hazard maps (Frankel et al., 1996; Petersen et al. 1996). The updated 2002 maps contain some major changes compared to the previous version (Frankel et al. 2002). Therefore, it is important to study the uncertainties of these maps and the sensitivities of the uncertainties to the model elements and seismic source parameters for understanding and using these new maps. From a scientific point of view, the uncertainty maps are inseparable part of seismic hazards that are as important as the hazard map themselves. It is also very useful to provide the uncertainty maps to the hazard map users and describe how we can reduce uncertainties in the future.

There are two types of uncertainties, model and random. Model uncertainties are also called the epistemic uncertainties (Reiter, 1990; Cao et al., 1996), which are the knowledge-based variability (Cramer, 2001a) of the seismic hazard model. Random uncertainty is called aleatory uncertainty and is the natural variability in earthquake source and ground shaking parameters. This uncertainty is considered explicitly in the hazard calculations (Reiter, 1990; Cao et al., 1996). The model elements define how the hazards are modeled, that include for example the attenuation relations selected and the fault rupture area-magnitude relations used. The model parameters are, for example, the weights for each attenuation relation and area-magnitude relation. Details of the 2002 update of the California hazard model are described in Frankel et al. (2002). We will highlight the model in next section using a logic tree. The sensitivity studies isolate the uncertainty contributions to each model element and parameter. In this study we are mostly interested in comparing the uncertainty contributions from each model element.

A Monte Carlo approach of randomly sampling the California seismic hazard logic tree is adopted in this study. This sampling method only provides the sample not the population uncertainties. We can make the inference from sample to population uncertainties through increasing the number of iterations. This approach was used to evaluate the uncertainties for the 1996 USGS national seismic hazard maps (Frankel et al., 1997). This approach was also applied to the uncertainty analysis of the seismic hazard assessment of Los Angeles, Ventura, and Orange counties (tri-county) (Cramer et al., 1996) and to the New Madrid seismic zone and Southern Illinois Basin (Cramer, 2001a, b; Cramer et al., 2002).

Some fundamentals on the Monte Carlo sampling method are discussed in this study because we are applying a sampling method different from some published studies. During the analysis of the obtained uncertainty maps, we found that it is very helpful to analyze some basic test cases first. These test cases of simple one-fault and two-fault systems are designed to explore the fundamental patterns of seismic ground motion uncertainties and their sensitivities. After exploring these test cases we calculated the uncertainty maps for the San Francisco Bay region in Northern California and the tri-county region in Southern California. These are not only the most populated and hazardous regions in California but we can also compare our results with previous

uncertainty analysis by McGuire and Shedlock (1981) for the Bay region and Cramer et al. (1996) for the tri-county region. Because of the richness of all type of seismic sources in the tri-county region, a detailed sensitivity analysis is performed to show the relative contributions of uncertainties from each model element. Finally the ground motion uncertainty map for the whole state is analyzed using the fundamental uncertainty patterns obtained from the test case studies.

Because similar uncertainty analysis has not been performed to the 1996 and earlier California hazard models we are unable to make conclusions that if the uncertainties have gone up or down with time. Comparing the mean hazards of other models with the 2002 model is beyond the scope of this study so we present uncertainty results using COV maps or curves in this study.

2002 California Seismic Hazard Logic Tree and Monte Carlo Sampling

In the 1996 California seismic hazard model, the sources are divided into three classes: A for active faults with rupture histories, B for active faults with unknown rupture histories, and C for areas with seismicity but no known active faults, respectively (Petersen et al., 1996; Cramer et al., 1996). The class A faults are modeled with pure characteristic recurrence processes. The class B faults are modeled with a combination of characteristic and Gutenberg-Richter (G-R) recurrence processes. These classifications and modeling are still used in the 2002 California model. But the 2002 model has more complexities compared to the 1996 model. Figure 1 is the logic tree for the 2002 California model, which is a version evolved from a preliminary version presented by Cramer et al. (2001b) at a user workshop convened by the Applied Technology Council (ATC) and the USGS in 2001. In Figure 1 the top row lists all the branch point titles, which are called model elements in the paper. The symbols in the parenthesis indicate the seismic sources for which the branch point title above and branches below apply. The only symbol not mentioned above is “BK”, which refers to the background seismicity (Cao et al., 1996). The historical seismicity in California is used with a Gaussian smoothing process to produce a gridded seismicity for hazard calculations for the background seismicity. The weights for the branches have been called model parameters in the last section. Three branch points (the fault length, width, and shear modulus) in the logic tree of Cramer et al. (1996) for tri-county, which together contribute to the magnitude uncertainty, are not included in Figure 1. It is because of their relatively small contributions to uncertainties (Cramer et al., 1996) and the new epistemic magnitude uncertainty branch point (Fig. 1), which well replaces those three branch points.

The differences between the 1996 and 2002 California hazard models are at almost every branch point in Figure 1. In the 1996 model different tectonics between eastern and western California are not distinguished; three attenuation relations (Boore et al., 1993; Campbell and Bozorgnia, 1994; Geomatrix, 1995) are used; only Wells and Coppersmith (1994) fault area-magnitude relation is used; no epistemic magnitude uncertainty is included; the moment release ratio between characteristic and G-R recurrence processes is 50% vs. 50%. In the 2002 model, there are two branches under the branch point title for fault area-magnitude relation. Each branch uses the Wells and Coppersmith (1994)

area-magnitude relation for fault rupture area smaller than 500 km². For rupture area greater than 500 km², one branch uses Ellsworth (WGCEP 2002 or WG02) formula and the other Hanks and Bakun (2002) formula. There are also some other important changes, which are not included in the logic tree of Figure 1, such as the multiple-segment cascade along Southern San Andreas fault, modeling of the creeping section of the San Andreas fault and Brawley seismic zone, the multiple models for the Cascadia subduction zone in northwest California, and the results of WG02, which is adopted in the 2002 model. We will add details to these changes when analyzing the uncertainty maps.

Different models represented by different branches of a logic tree can be sampled using a Monte Carlo method. The weight of each model is determined by the weights of branches under all branch point titles. Let us use five integers i, j, k, l, m to denote the branches selected from five branch points in Figure 1. Uncertainty in slip rate is modeled with a truncated normal distribution, which is discretized. In the following we assume it is discretized to 7 bins. A class B fault modeled by a combination of five branches from five branch points, which are specified by those five integers, produces a hazard curve at a particular site. The hazard curve is the annual frequency of exceedance (AFE) as a function of peak ground accelerations (PGA) or spectral accelerations at certain period. Each hazard curve for a specific sampled model can be expressed as $f_{i,j,k,l,m}(g)$, where g is PGA or spectral acceleration. The mean hazard curve (it is a population mean) can be expressed as

$$f_0(g) = \sum_{i,j,k,l,m=1}^{ix,jx,kx,lx,mx} w_i^a w_j^b w_k^c w_l^d w_m^e f_{i,j,k,l,m}(g) \quad (1)$$

where a, b, c, d , and e denote the five branch points and $w_i^a, w_j^b, w_k^c, w_l^d$, and w_m^e denote the five weights for five branches selected from five branch points. The integers ix, jx, kx, lx , and mx denote the total number of branches for each of the five branch points. They are 4 (or 5), 2, 3, 2, and 7 respectively in the California logic tree (Fig. 1). If there is more than one fault source, one more summation will be added to sum up all the fault sources. The Monte Carlo sampling randomly generates these five integers in each Monte Carlo realization with the probability of each integer being generated is equal to the weight in (1) for a particular branch. When the number of simulations is large enough, the sample mean of sampled hazard curves will be approaching the population mean of (1).

In each Monte Carlo realization of Cramer et al. (1996), all the faults share the same set of integers. This means that if a generated integer happens to select the characteristic model, then all the faults will be modeled as characteristic. From physical point of view, we think this type of dependence between faults is not necessary. The attenuation relation is an exception because all the attenuation relations used were developed for western U.S. So in this study we apply a different Monte Carlo sampling, in which only the selection for attenuation relation is the same for all faults in a particular realization. All other four selections for area-magnitude relation, epistemic magnitude uncertainty,

characteristic or G-R modeling, and slip rate branches in the logic tree are random or independent from fault to fault. In the next section we will show that this independent sampling reduces the uncertainties compared to the dependent sampling.

Let us show that if we are studying the uncertainties from one or any number of branch points (sensitivity studies) the mean hazard curve is always the same as (1). Assume we want the uncertainty from attenuation relations only. Then all the branches in each branch point are averaged except the branch point for attenuation relations. The Monte Carlo sampling is now selecting i only and will produce the following hazard curves:

$$f_i^a(g) = \sum_{j,k,l,m=1}^{jx,kx,ix,mx} w_j^b w_k^c w_l^d w_m^e f_{i,j,k,l,m}(g) \quad (2)$$

where the index i is from 1 to ix or 4 for faults in the extensional tectonic zone. Since the probability to select hazard curve $f_i^a(g)$ is w_i^a the (sample) mean hazard curve from sampling i only is approaching the following population mean

$$f_0^a(g) = \sum_{i=1}^{ix} w_i^a f_i^a(g) = f_0(g) \quad (3)$$

In the sensitivity studies we evaluate the uncertainties from each model element (branch point in Fig. 1). Relation (3) provides a common basis for sensitivity studies that all the uncertainty evaluations refer to the same mean hazard curve and therefore the same mean ground motions. Without this common basis the uncertainties are less compatible. Formula (1) becomes the exact expression for the 2002 California mean hazard calculation if the summation to the discretized fault slip rate distribution is removed and a mean slip rate is used.

The above discussion leads to another issue, which is how to get the ground motion uncertainty from a group of sampled hazard curves. A common practice (Coppersmith and Youngs, 1986; Cramer, 2001c) is to calculate the ground motion value for each hazard curve for a given risk value (for example, 0.0021 for 10% exceedance in 50 years) first. Then calculate the mean, standard deviation (STD), and coefficient of variation (COV) from the ground motion values. Figure 2 is a sample for studying the uncertainties from a single fault source with only two model elements, characteristic vs. G-R modeling and area-magnitude relations, which provide two different magnitudes M1 and M2. The hazard curves f1, f2, f3, and f4 are from the models of four combinations: characteristic and M1 (f1), characteristic and M2 (f2), G-R and M1 (f3), and G-R and M2 (f4). Assuming each curve (model) has a weigh of 0.25, f0 is the mean hazard curve. For a risk value of 0.0003 we can get four PGA values labeled by 1, 2, 3, and 4 in Figure 2. The problem happens at relatively high-risk values. At risk value 0.0021 we see that curve f1 does not provide a unique non-zero ground motion value. The mean PGA at risk value 0.0021 obtained by averaging four PGA values can be different from the mean PGA from the mean hazard curve f0.

If we want to study the uncertainty from characteristic vs. G-R modeling only, curves f1 and f2 are averaged on AFE to obtain curve f12; curves f3 and f4 are averaged on AFE to obtain curve f34. Following the common approach the mean PGA is from these two averaged hazard curves f12 and f34. For risk value of 0.0021 both these curves have non-zero PGA values and the mean is obviously different from the previous one, which is obtained from four hazard curves. So the common approach does not consistently evaluate the mean PGA and its STD at low ground motion or high risk value range. In this study we use a different approach to calculate the mean ground motion values and uncertainties. Our approach calculates the mean hazard curve and the STD of AFE (not the STD of PGA) first. Then the mean PGA is from mean hazard curve and the STD of PGA from the STD of AFE. Finally we calculate the COV of PGA from the STD and mean of PGA. If we think the different hazard models from Monte Carlo sampling are like different fault sources then we see our approach is consistent with how the hazards are summed up in the 2002 hazard model calculations. We compared the above two approaches and found they produce very close results in most cases and different results at $PGA < 0.5$ g. Our approach averages hazard curves in the vertical direction. Actually it faces similar problem like the common approach, which averages hazard curves in the horizontal (ground motion) direction, at very low risk values or very high ground motion values that are not affecting the uncertainties shown in this study for 10% of exceedance in 50 years (risk value 0.0021).

The uncertainties from Monte Carlo simulations are the sample uncertainties not the population uncertainties. In order to make the inference from sample uncertainties to population uncertainties, such as from sample COV to population COV, that is the basis for the conclusions of this study, we tested the number of Monte Carlo simulations or realizations needed by plotting the 2nd, 16th, 50th, 84th, and 98th percentile values of AFE values as a function of the number of simulations. We confirmed Cramer et al.'s (1996) result that a minimum of 100 simulations is needed to obtain estimates of AFE uncertainty within 5% of each other for different starting points of random number generations. We also tested much high numbers of iterations (400-800) for a small area in tri-county region. This minimum number depends on the complexity of the logic tree or the total number of branches. The logic tree (Fig. 1) for the 2002 California model is very similar to Cramer et al. (1996) in complexity. Because the 2002 California hazard model is Poissonian all the faults are independent to each other and increasing the number of faults in a system will not increase the minimum number of iterations required. For example, a system containing 100 class B faults requires the same minimum number of iterations as a system containing only one fault. But in each iteration the former samples the same logic tree (Fig. 1) 100 times and the latter only once. We used the number 150 for all the regional simulations and 400 for all the test cases in this study.

Ground Motion Uncertainties of One-Fault and Two-Fault Systems

In order to study the fundamental patterns of hazard model uncertainties four basic test cases are designed (Fig. 3). Case 1 is to show how ground motion uncertainties change with distance from a fault and what is the uncertainty sensitivity for each model element. Case 2 is to explore how uncertainty and sensitivity change with fault magnitude. Case 3 is designed so that the results can be compared with Case 4. Case 4 is to show why the COV values of ground motions from two nearby faults are lower than from one fault in Case 3.

Case 1 is for a class B fault with moderate magnitudes (6.8 – 7.0) in the non-extensional tectonic region (Fig. 3). The distance is measured from point A on the fault along a line AB perpendicular to the fault. The COV of PGA for risk value 0.0021 along line AB is shown in Figure 4. The COV value due to all five model elements (branch points in Fig. 1) decreases with distance from the fault to a minimum value around 45 km and then increases to higher than around the fault. The sensitivity analysis, in which the COV value due to each model element is evaluated, shows that the COV value decreasing and then increasing is due to the uncertainty of attenuation relations, which dominates the total uncertainty at this magnitude level. Figure 5 plots all the attenuation relations (M 7.0) used in the 2002 California hazard model for the non-extensional tectonic region. It is obvious that the data used to develop these relations have better constraints at distances around 40 to 50 km where most data is grouped. McGuire and Shedlock (1981) found this pattern of COV decreasing and then increasing first and also attributed to the uncertainties of attenuation relations. At large distances from the fault the COV values are high but the ground motion values and its STD are all low. If there is a local fault at such large distance the high COV from the first fault will be overwhelmed by the COV of the second fault because the ground motions are dominated by the later. Figure 6 shows the same analysis like in Figure 4 but for a much lower risk value 0.0004, which is for 2% of exceedance in 50 years. Every COV curve in Figure 6 is lower than in Figure 4. The COV values for the uncertainties of attenuation relations decrease the least from Fig. 4 to Fig. 6. This result of COV value decreasing with lowering risk value following the same hazard curve is due to the nature of probabilistic hazards. We call it a hazard effect and will be used to explain the result of Case 4.

Case 2 is for a longer class B fault with magnitude 7.5 from both area-magnitude relations (Fig. 3). Every COV curve of this case (Fig. 7) for PGA at risk value 0.0021 is higher than in Case 1 (Fig. 4). The COV values for the uncertainties of attenuation relations increase the least and the COV values for the characteristic vs. G-R modeling increase the most. The uncertainty due to the characteristic vs. G-R modeling now dominates the total uncertainties. This uncertainty does not have a pattern of decreasing and then increasing from the fault, therefore, the COV curve for total uncertainties decreases with distance from the fault and then levels off without creating a trough. Figure 8 shows the four hazard curves of Cases 1 and 2 at site A for characteristic and G-R models respectively. It shows that a longer fault with high magnitude 7.5 (Case 2) has a much longer recurrence time than a shorter fault with the same slip rate but lower magnitude 7.0 (Case 1). Figure 8 shows that the long fault has lower hazards than the short fault at all risk values and in both cases the G-R model predicts higher hazards than the characteristic model. It also shows that for a risk value of 0.0021 the difference in

PGA hazard between characteristic and G-R modeling is much larger for M 7.5 than for M 7.0. This explains why the uncertainty due to characteristic vs. G-R modeling in Case 2 (Fig. 7) is dominant. But the difference in PGA or AFE values between characteristic and G-R modeling decreases with lowering risk values or longer return periods. Because class A faults are not modeled with different area-magnitude relations and are modeled with characteristic recurrence only, the COV value pattern of decreasing and then leveling off in Case 2 does not apply even for large magnitude class A faults. The pattern in Case 1 applies to class A faults.

Case 3 is not much different from Case 1 except the line AB (Fig. 3) is no longer perpendicular to the fault. The angle between line AB and the fault is 58 degrees. (It looks less than 58 degrees in Figure 3 because the scales for vertical and horizontal axes are different.) In Case 4 a mirror image of the fault in Case 3 is added so we can study how the hazards and uncertainties are changed from Case 3. Figure 9 shows the mean hazard curves (f_1^0 and f_2^0) and the mean +/- STD curves (f_1^+ , f_1^- , f_2^+ , and f_2^-) at site A for Cases 3 and 4 respectively. According to a basic rule of statistics the mean value of a sum of random variables equals the sum of the mean values. So we should expect the AFE value at a given PGA on curve f_2^0 is twice the value on curve f_1^0 , which is confirmed by our simulations. It simply means that the annual frequency of exceedance in Case 4 is doubled from Case 3 because we have two symmetric faults contributing hazard to site A. According to another rule of statistics that the variance (the square of the standard deviation) of a sum is equal to the sum of the variances for independent variables. So we should expect the variance of Case 4 is also doubled from Case 3. But now the COV of AFE in Case 4 is the COV in Case 3 multiplied by a factor of $\sqrt{2}/2 = 0.707$ or about a 30% decrease. Our simulation also confirmed this result. For example, at PGA value 0.4 g, the mean AFE values are 0.0022 and 0.0043 for Cases 3 and 4 respectively; the COV values for AFE are 0.59 and 0.43 for Cases 3 and 4 respectively (Fig. 9). But if we use the dependent sampling, in which two faults share the same selections of model elements (branch points) the COV of AFE is not decreased from Case 3 to Case 4. It is because the variance for two dependent faults is four times of one fault. Our simulations also confirm this. In Figure 9, the line for risk value 0.0021 crosses the one-fault mean hazard curve f_1^0 at P1 at PGA value around 0.45 g. Now for the same PGA value, the AFE value is doubled at point P2 on the mean hazard curve f_2^0 for the two-fault system. But the COV of AFE at P2 decreases by 30% from P1. This decrease of COV values by adding another independent variable is due to the statistical nature of random variables. We call it a statistical effect.

We are usually interested in the uncertainties of ground motions at a given risk value. That the COV value decreases from points P1 to P2 (Fig. 9) is not the decrease we will see on an uncertainty map at a location with two or more faults close to each other because the risk value at P2 is different from at P1. What we will see is the COV value changes from point P1 to point P3 (Fig. 9) for the same risk value. P3 is the cross point between the line of risk value 0.0021 and the mean hazard curve f_2^0 for the two-fault system in Case 4. We just showed that the COV value of AFE at P3 is 30% lower than at

P4 on curve f_1^0 due to the statistical effect. We also showed in Case 1 that the COV value decreases with lowering risk value (longer return period) following the same hazard curve from point P1 to point P4 due to the hazard effect. So the COV value at P3 is the value at P1 multiplied by two decreasing factors: first from point P1 to point P4 due to the hazard effect and second from P4 to P3 due to the statistical effect.

Figure 10 compares the COV of PGA between Cases 4 and 3. The PGA and STD values are also shown. We see that the PGA values increase from a one-fault system to a two-fault system but is not doubled like AFE values. The COV and STD values of PGA both decrease due to the statistical and the hazard effects. It is interesting to note that the STD for the two-fault system is lower than the one-fault system. This is due to the hazard effect. Without the hazard effect, the STD of AFE for a two-fault system should be higher than the one-fault system by a factor of $\sqrt{2}$. For STD of PGA it should be higher too without the hazard effect. The hazard effect and statistical effect become negligible when faults are far apart to each other because in the area near a fault the COV values are dominated by the fault itself.

In this section we have shown through basic test cases for class B faults that the COV of PGA decreases with distance from a fault and then increases for faults with moderate magnitudes (Cases 1); for class B faults with large magnitudes the COV decreases with distance from the fault and then levels off (Case 2); if two or more faults are close to each other the COV values of AFE or ground motions decrease to lower than for one fault alone in the area near both faults. These are general and qualitative uncertainty patterns and will help us to analyze the uncertainty maps in the following sections. The quantitative estimation of decrease or increase of COV values with distance from a fault and the decrease of COV values due to adjacent faults depend on the fault geometries, magnitude, and slip rate.

Uncertainties for the San Francisco and Tri-County Regions and Sensitivity analysis for the Tri-county Region

The San Francisco Bay and Southern California tri-county regions are heavily populated with very high seismic hazards. These two regions are also rich in all types of faults such as the well defined class A faults and the poorly defined blind thrust faults beneath the Los Angeles and San Francisco basins, the western Transverse Ranges, and the Santa Barbara Channel. Therefore, we compute uncertainty and sensitivity using finely spaced grid (0.05 degree).

Figure 11 is a fault map for the tri-county region and Figure 12 is the map of COV for PGA (10% exceedance in 50 years) in the same region. In the California logic tree (Fig. 1), the cascade models for Southern San Andreas fault are not included but are sampled in the Monte Carlo simulations according to the model weights described in Appendix A of Frankel et al. (2002). In order to compare with the early studies of Cramer et al. (1996) we also did not include the hazards due to background seismicity. The mean hazards used to calculate COV are from fault sources only. The contour interval is 0.05.

The COV values along the San Andreas fault is around 0.15 and decreases on both sides to 0.1 then increases to 0.2 to 0.3, where the class B faults are located. This pattern of COV decreasing with distance from the fault and then increasing is typical, as we have shown in test Case 1. The COV value does not keep increasing to a value like 0.4 to 0.5. Instead, it is overwhelmed by other fault sources. There are three high COV areas, which are around the Garlock, Anacapa-Dume, and Palos Verdes faults. These are the poorly defined faults with high magnitudes. They belong to the test Case 2 type faults. The high COV values are mostly due to the high magnitudes, which lead to very different ground predictions between characteristic and G-R modeling. These faults are also relatively isolated with no nearby faults to jointly bring the COV value down through statistical and hazard effects.

The general pattern of this COV map is similar to Cramer et al. (1996) with one major difference which is that the uncertainties along class A faults are lower than along class B faults in this study. From the logic tree (Fig. 1), we expect the class A faults to have lower uncertainties than the class B faults. The class A faults do not have uncertainties from area-magnitude relations and characteristic vs. G-R modeling (they are 100% characteristic). The fault slip rate uncertainties (COV) for class A faults are always lower than for class B faults. Another different observation in Figure 12 is that the contours along the Garlock fault, Mojave and Carrizo segments of the San Andreas fault all make a U-turn when they get close to each other. This phenomenon also happens near the southeast end of Mojave segment, where the San Jacinto fault, San Bernardino and Mojave segments of the San Andreas fault get close to each other. The low COV areas between those contours are due to the statistical effect and hazard effect shown in test Case 4. The COV values in the central part of the region (Figs. 11 and 12), where many faults are close to each other, are in the range of 0.2 to 0.3 not 0.4 to 0.5 is also partly due to the statistical and hazard effects. Those isolated faults mentioned above become outstanding with high COV values because there are no nearby faults to cause significant statistical and hazard effects. These two effects may also partly explain high COV values in eastern and central U.S., where in many cases only one major fault system dominates the hazards.

Figures 13a to 13e are for sensitivity analysis using COV of PGA (all at 10% of exceedance in 50 years). These figures show how each of the five model elements (five branch points in Fig. 1) contributes uncertainty to the total uncertainties shown in Figure 12. The relative contributions among these figures are very consistent with the results in Cases 1 and 2. The attenuation relations (Fig. 13 a) contribute most of the uncertainties as shown in Case 1 (Fig. 4) except for the Garlock, Anacapa-Dume, and Palos Verdes fault areas, where the uncertainties due to characteristic vs. G-R modeling (Fig. 13e) become dominant as shown in Case 2. The uncertainties due to epistemic magnitude uncertainty (Fig. 13b), fault slip rate uncertainty (Fig. 13c), and area-magnitude relations (Fig. 13d) are all relatively small as shown in test Case 1 (Fig. 4).

The uncertainties from the background seismicity are due to the attenuation relations (Fig. 1) and the incompleteness of seismic catalogs (Cao et al., 1996). The latter is not shown in the logic tree (Fig. 1) but counted in this study by resampling the catalogs.

Figure 14 shows the map of COV for PGA from background seismicity. The mean hazards used to calculate COV here is different from Figures 12 and 13. In Figures 12 and 13, the mean hazards are from all fault sources only; in Figure 14 the mean hazards are from fault and background sources together. So the mean hazards in the latter are close to the 2002 update of California mean hazards to within a few percent differences. Figure 14 shows that the uncertainties due to background seismicity are insignificant compared with the uncertainties from other model elements. The contours show some influences from the major faults in this area. As expected, it is a reversed influence that there are no or very low uncertainties at the fault locations because the background seismicity is mostly distributed off the faults.

Figure 15 is a fault map for the San Francisco Bay region. In the 1996 model (Petersen et al., 1996) only San Andreas and Hayward faults are classified as class A faults and the others are class B faults. But we may expect lower uncertainties from these class B faults that have been updated to class A faults due to the studies of WG02. In the 2002 update of California hazard the results from WG02 were adopted. For uncertainty analysis we also use the WG02 results on uncertainties instead of using the logic tree (Fig. 1). The attenuation relations used for this region are the same as in the logic tree for non-extensional tectonics (Fig. 1). Figure 16 is the COV map for PGA at 10% of exceedance in 50 years. Since this map covers far enough into the ocean, where there are no seismic sources included in the 2002 hazard model, the COV contours show a clear trend of decrease with distance from the faults and then increasing to the west. The COV values along the class A faults and those class B faults studied by WG02 are 0.1 to 0.15, which are the same as for the tri-county region in Southern California. The COV values around class B faults in this region are lower than in tri-county because of the work of WG02 and are now similar to A faults. The very high COV values at Maacama fault area are mostly due to the characteristic vs. G-R modeling as shown in test Case 2. The COV value decrease due to statistical and hazard effects also can be found between the Maacama and Rodgers Creek faults, in the area where the Green Valley, Concord, Greenville, Calaveras, Mt. Diablo, and Hayward faults are close to each other. The COV values in this region are about half of the values obtained by McGuire and Shedlock (1981). Cramer et al. (1996) attributed the higher COV values of McGuire and Shedlock (1981) to the use of discrete distributions with large variances.

California Ground Motion Uncertainty Map

For creating the California probabilistic ground motion (PGA) uncertainty map (COV of PGA) we have to include some seismic sources, which are not included in the California hazard logic tree (Fig. 1). These are the sources in the Cascadia subduction zone, the northern California deep earthquake zone (depth > 35 km), the shear zones, and Nevada, where the seismic sources contribute to the California hazards. In the 2002 California hazard model four different eastern edges of rupture zone are used for the Cascadia subduction zone. Three of them are based on the work of Fluck et al. (1997) with weights of 0.1, 0.2, and 0.2 (Frankel et al., 2002). The fourth one is revised from the

1996 model (Frankel et al., 1996; Petersen et al., 1996) with a weight of 0.5. Floating earthquakes with magnitudes 8.3 and 9.0 are placed on these rupture zones. To evaluate the ground motion uncertainties from these floating events the magnitude uncertainty is set to +/- 0.1; the variation of a-value, which is a seismicity rate in the G-R magnitude frequency relation, is obtained using the aperiodicity value of 0.58 from Petersen et al. (2002). This value is derived with limited paleoseismic data and a time-dependent recurrence model, which has a log-normal density function for the recurrence intervals. The deep seismicity in northern California is modeled differently from the background seismicity in the rest of California. There are two alternative models weighted equally, one uses two attenuation relations: in-slab and in-slab with Cascadia corrections (Atkinson and Boore, 2002); the other uses only one attenuation relation (Youngs et al., 1997). To avoid a sudden drop of uncertainty due to one attenuation relation in the second model, an artificial variation of 15% according to the variation in the first model is added to the second model. The fault slip rate uncertainties for Nevada faults are not available yet so the uncertainty contributions from Nevada faults are calculated without slip rate uncertainties.

Figure 17 is the California COV map for PGA at 10% of exceedance in 50 years. The uncertainties from background seismicity are also included so the mean hazards are close to the 2002 update of California mean hazard to within a few percent. This map is calculated with a grid spacing of 0.1 degree. For the San Francisco Bay and tri-county regions some of the details shown in Figures 12 and 16 may be less clear here. Because of the added uncertainties due to background seismicity the uncertainties for the Bay and tri-county regions are not exactly the same as shown in Figures 12 and 14. However, we find that all the observed patterns of spatial uncertainty distributions and the relations with faults for the Bay and tri-county regions are even more clearly seen on the state uncertainty map. The COV values along the class A faults are around 0.1 to 0.15 from southern to northern California following mostly the San Andreas fault system. The COV values around class B faults, which are located mostly on both sides of the class A faults, are higher at around 0.2 to 0.3. The pattern of COV values decreasing with distance from a fault and then increasing with distance beyond 50 km are also shown along every fault. It is interesting to note that the increase of COV values from the California fault system, in which most of the faults have a northwest to southeast strike direction creates a COV contour pattern to the west of California into the Pacific ocean. Because the 2002 California hazard model does not have seismic sources, even background seismicity, far into the ocean the increasing pattern revealed in test Case 1 is not interrupted. To the east of the San Andreas fault system such a pattern is not observed because of the interruptions from fault sources in eastern California and Nevada and also the background seismicity. The decrease of COV values due to the statistical and hazard effects is also observable at many places where multiple faults or fault segments are close to each other.

Other than those faults highlighted in the last section, high COV values are also observed at the Cascadia subduction zone in northern California, and around the Owens Valley fault in eastern California. The high COV values around the Garlock and Maacama faults, partially shown in Figures 12 and 16, are now shown along their entire lengths

(Fig. 17). All these faults having high uncertainty values around them share some common features: they produce large magnitude earthquakes with long recurrence times; they are poorly defined; they are not joined by nearby faults to have uncertainties reduced through the statistical and hazard effects. Fortunately, they are all located in less populated areas.

Summary and Discussions

In this study we proposed to use an independent sampling among faults in each Monte Carlo simulation. The COV values of annual frequency of exceedance and ground motions obtained using independent sampling are lower than the dependent sampling due to the basic statistical feature of probabilistic hazards. For high risk values or low ground motion values, we also proposed to use hazard curves from Monte Carlo sampling to calculate the mean hazard curve and the uncertainty of annual frequency of exceedance for all simulated hazard curves first. The ground motion uncertainty is calculated from the AFE uncertainty. In the common approach, the ground motion uncertainty is calculated directly using the ground motion values from each sampled hazard curve for a given risk value. The common approach may drop some of the simulations for which the annual frequency of exceedance is lower than the given risk value at relatively low ground motion levels (< 0.5 g). Because of the missing count to some of the simulations this common approach does not have consistent mean hazards for sensitivity analysis at low ground motion values or high risk values. Our numerical tests showed the difference between these two approaches happen only at very high and low ground motion values.

Using the independent sampling for Monte Carlo simulations and the different approach for evaluating ground motion uncertainties, we calculated the uncertainties (COV) for four designed test cases. From these test cases we showed the basic features or patterns of uncertainties for systems containing one fault and two faults. We found that for faults with moderate magnitudes ($M \sim 7.0$), the COV of ground motion decreases at short distance from a fault and then increases with distance beyond 50 km. The trough bottom is located around 40 to 50 km from the fault where most of the strong motion data is grouped. In this case the attenuation relations dominate the uncertainty. When increasing the return periods (lower risk values) and keeping the magnitude and fault slip rate unchanged, the COV of ground motions decreases significantly; but when increasing the fault magnitude and keeping the return period and fault slip rate unchanged, the COV increases significantly. At high fault magnitudes ($M \sim 7.5$) the COV increase is mostly due to the characteristic vs. G-R modeling.

In the two-fault system test, the annual frequency of exceedance is doubled as compared with the one-fault system but the COV of AFE decreases due to the statistical effect. The COV of AFE decreases even more if the risk value is unchanged due to the hazard effect that the uncertainty decreases with lowering risk value along a hazard curve. Because of these two effects the COV values decrease within an area, where more than one fault or fault segment are close to each other. This happens very often in California.

The California COV map for PGA at 10% exceedance in 50 years shows all the features or patterns discussed above. In the future, the hazard maps will evolve but these general patterns of uncertainty (COV) will remain the same because they result from generic one-fault and two-fault systems. The COV along the class A San Andreas fault system is 0.1 to 0.15, which is lower than the value 0.2 to 0.3 along the class B faults. COV values decrease from class A faults to 0.1 or less then increase to 0.3 or higher to the west direction, where there are no seismic sources that will overwhelm the increase. To the east, the increase is interrupted by the local seismic sources in the Great Valley, eastern California, Nevada, and by background seismicity. The COV values in the great valley and eastern California are about 0.05 to 0.1. Much higher COV values (0.4 to 0.6) are located around the Garlock, Anacapa-Dume, and Palos Verdes faults in southern California and the Maacama fault and Cascadia subduction zone in northern California.

We tested the difference between the (sample) mean hazard values from Monte Carlo simulations and the 2002 update of California mean hazards, which are calculated using mean parameters of the model directly without Monte Carlo simulations. We found the differences in ground motions (10% of exceedance in 50 years) are smaller than a few percent (mostly smaller than 1%). This confirms the conclusion of McGuire and Shedlock (1981) that the parameter uncertainties need not be considered in hazard analysis for the estimate of mean hazards.

The results on hazard uncertainties in the 2002 update of the California hazard model may be useful to the engineers for better determining the safety factor in the building and structural designs. The uncertainty results may also help the insurance rate determination, which largely depend on using the hazard maps and their uncertainties. One of the fast developing applications of the hazard maps is the loss estimation, which will benefit greatly from the uncertainty analysis of this study (Cao et al., 2000; Wesson et al., 2001). This study provides a reference point for the future studies to determine how much the hazard uncertainties have decreased due to the efforts on evaluating California seismic hazards in the past decades. It also provides a reference point for the comparisons of the mean hazards and their standard deviations between the 2002 model and other earlier models.

Acknowledgements

The authors are grateful to William Bryant and Jerome Treiman for providing us the fault data. We thank Chris Cramer, Robert Wesson, David Perkins, Stephen Harmsen, and Chris Wills for helpful discussions. This study is supported by the USGS/NEHRP grant 04HQGR0027.

REFERENCES

Abrahamson, N.A. and W.J. Silva (1997). Empirical response spectral attenuation relations for shallow crustal earthquakes, *Seis. Res. Letts.*, v. 68, no.1, pp. 94-127.

- Atkinson, G.M. and D.M Boore (2002). Empirical ground-motion relations for subduction zone earthquakes and their application to Cascadia and other regions, in review.
- Boore, D.M., W.B. Joyner, and T.E. Fumal (1993). Estimation of response spectra and peak acceleration from western North American earthquakes: an interim report, *U.S. Geol. Surv. Open-File Rept.* 93-509.
- Boore, D.M., W.B. Joyner, and T.E. Fumal (1997). Equations for estimating horizontal response spectra and peak acceleration from western North American earthquakes: a summary of recent work, *Seism. Res. Letts .*, v. 68, pp.128-153.
- Campbell, K.W. and Y. Bozorgnia (1994). Near-source attenuation of peak horizontal acceleration from worldwide accelerograms recorded from 1957 to 1993, in Proc. of the Fifth U.S. National Conference on Earthquake Engineering, July 10-14, 1994, Vol. 3, Chicago, Illinois, Earthquake Engineering Research Institute, Oakland, California, 283-292.
- Campbell, K.W. and Y. Bozorgnia (2003). Updated near-source ground motion attenuation relations for the horizontal and vertical components of peak ground acceleration and acceleration response spectra, *Bull. Seism. Soc. Am.*, 93, pp.314-331.
- Cao, T., M.D. Petersen, and M.S. Reichle (1996). Seismic hazard estimation from background seismicity in southern California, *Bull. Seism. Soc. Am.* 86, pp. 1372-1381.
- Cao, T., M.D. Petersen, C.H. Cramer, T.R. Topozada, M.S. Reichle, and J.F. Davis (2000). The calculation of expected loss using probabilistic seismic hazard, *Bull. Seism. Soc. Am.*, 89, pp. 867-876.
- Coppersmith, K.J. and R.R. Youngs (1986). Capturing uncertainty in probabilistic seismic hazard assessment within intraplate tectonic environments, *Proceedings of the Third U.S. National Conference on Earthquake Engineering, Charleston, SC*, 301-312.
- Cramer, C.H. (2001a). The New Madrid seismic zone: Capturing variability in seismic hazard analysis, *Seismological Research Letters* 72, 664-672.
- Cramer, C.H., M.D. Petersen, and A.D. Frankel (2001b). Monte Carlo analysis for assessing uncertainty in national hazard maps (abstract), workshop by Applied Technology Council (ATC-35) and the USGS, May, 2001.
- Cramer, C.H. (2001c). Aseismic hazard uncertainty analysis for the New Madrid seismic zone, *Eng. Geology* 62, 251-266.
- Cramer, C.H., R.L. Wheeler, and C.S. Mueller (2002). Uncertainty analysis for seismic hazard in the Southern Illinois Basin, *Seismological Research Letters*, 73, 792-805.
- Cramer, C.H., M.D. Petersen, and M.S Reichle (1996). A Monte Carlo approach in estimating uncertainty for a seismic hazard assessment of Los Angeles, Ventura, and Orange counties, California, *Bull. Seism. Soc. Am.* 86, pp. 1681-1691.
- Fluck, P., R.D. Hyndman, and K. Wang (1997). Three-dimensional dislocation model for great earthquakes of the Cascadia subduction zone, *J. Geophys. Res.*, 102, pp. 20, 539-20,550.
- Frankel, A.D., S. Harmsen, C. Mueller, T. Barnhard, E.V. Leyendecker, D. Perkins, S. Hanson, N. Dickman, and M. Hopper (1997), USGS national hazard maps:

- Uniform hazard spectra, de-aggregation, and uncertainty, Proceedings of FHWA/NCEER Workshop on the National Representation of Seismic Ground Motion for New and Existing Highway Facilities, *NCEER Technical Report 97-0010*, pp. 39-73.
- Frankel, A., C. Mueller, T. Barnhard, D. Perkins, E. Leyendecker, N. Dickman, S. Hanson, and M. Hopper (1996). National seismic-hazard maps: documentation June 1996, *U.S. Geological Survey, Open-file Report 96-532*, 110 pp.
- Frankel, A.D., M.D. Petersen, C.S. Muller, K.M. Haller, R.L. Wheeler, E.V. Leyendecker, R.L. Wesson, S.C. Harmsen, C.H. Cramer, D.M. Perkins, and K.S. Rukstales (2002). Documentation for the 2002 Update of the National Seismic Hazard Maps, *U.S. Geological Survey, Open-file Report 02-420*, 33 pp.
- Geomatrix Consultants (1995). Seismic design mapping state of Oregon, Final Report, prepared for the Oregon Department of Transportation, Salem, Oregon.
- Hanks, T.C. and W.H. Bakun (2002). A bilinear source-scaling model for $M - \log A$ observations of continental earthquakes, *Bull. Seism. Soc. Am.*, 92, pp. 1841-1846.
- McGuire, R.K. and K.M. Shedlock (1981). Statistical uncertainties in seismic hazard evaluation in the United States, *Bull. Seism. Soc. Am.*, 71, pp. 1287-1308.
- Petersen, M.D., W.A. Bryant, C.H. Cramer, T. Cao, N.S. Reichle, A.D. Frankel, J.J.Lienkaemper, P.A. McCrory, and D.P. Schwartz (1996). Probabilistic seismic-hazard assessment for the state of California, *California Division of Mines and Geology Open-File Report 96-08*, *U.S. Geological Survey Open-File Report 96-706*.
- Petersen, M.D., C.H. Cramer, and A.D. Frankel (2002). Simulation of seismic hazard for Pacific Northwest of the United States from earthquakes associated with the Cascadia subduction zone, *Pure appl. Geophys.* 159, 2147-2168.
- Reiter, L. (1990). *Earthquake Hazard Analysis: Issues and Insights*, New York, Columbia University Press.
- Sadigh, K., C.Y. Chang, J. Egan, F. Makdisi, and R. Youngs (1997). Attenuation relationships for shallow crustal earthquakes based on California strong motion data, *Seism. Res. Letts.*, v. 68, pp. 180-189.
- Spudich, P., W.B. Joyner, A.G. Lindh, D.M. Boore, B.M. Margaris, and J.B. Fletcher (1999). SEA99: A revised ground motion prediction relation for use in extensional tectonic regimes, *Bull. Seism. Soc. Am.*, 89, pp. 1156-1170.
- Wells, D.L. and K.J. Coppersmith (1994). New empirical relationships among magnitude, rupture length, rupture width, and surface displacements, *Bull. Seism. Soc. Am.*, 84, pp. 974-1002.
- Wesson, R.L. and D.M. Perkins (2001). Spatial correlation of probabilistic earthquake ground motion and loss, *Bull. Seism. Soc. Am.*, 91, pp. 1498-1515.
- Working Group on California Earthquake Probabilities (2002). Earthquake probabilities in the San Francisco Bay region: 2002-2031 —*U.S. Geological Survey Circular 1189*, in review.
- Youngs, R.R., S.J. Silva, and J.R. Humphrey (1997). Strong ground motion attenuation relationships for subduction zone earthquakes, *Seism. Res. Letts.*, V. 68, no. 1, pp. 58-73.

CALIFORNIA LOGIC TREE

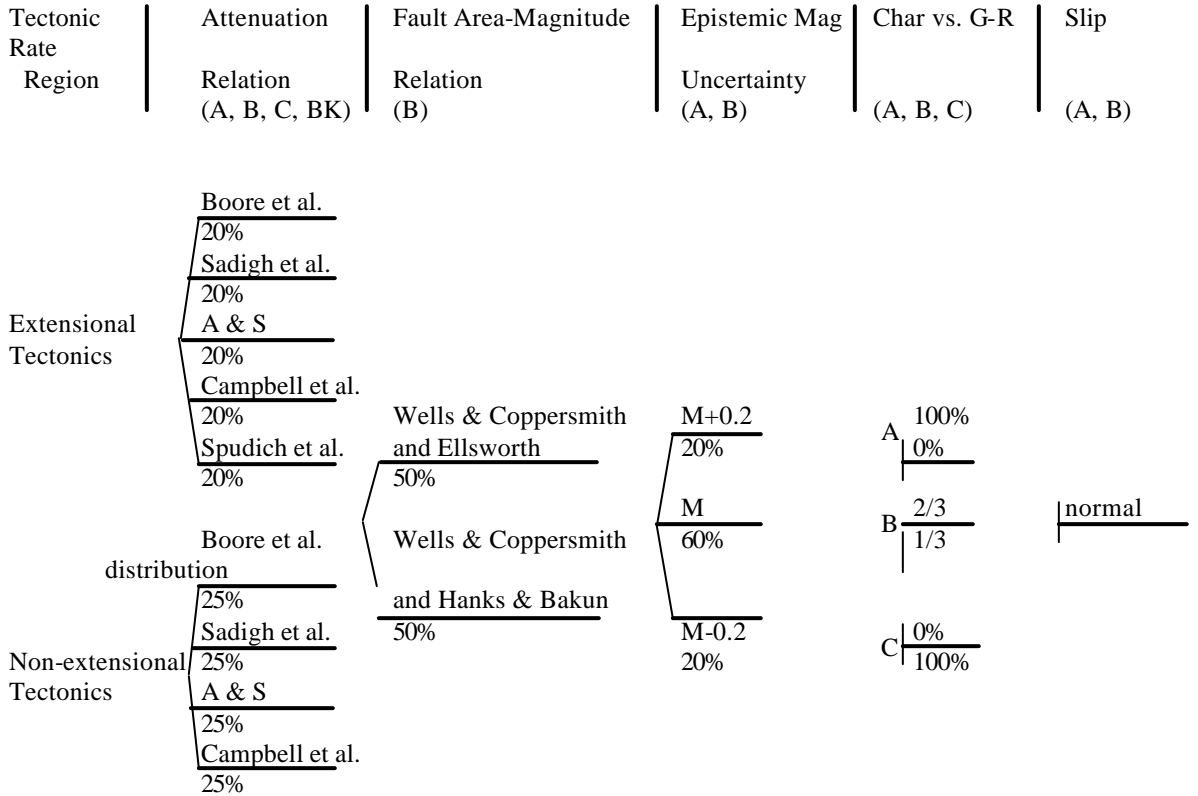


Figure 1. Partial logic tree for the 2002 update of California seismic hazard model. The subduction zone sources are not included here. The symbols in the parentheses under the branch point titles indicate the seismic source types applicable to the branch points above. They are “A” for class A faults, “B” for class B faults, “C” for area seismic zones with no known active faults, and “BK” for background seismicity. The abbreviated branch point title “Char vs. G-R” is for characteristic vs. Gutenberg-Richter modeling of the fault recurrence processes. The branch points are called model elements in the text; the weight for each branch is referred as model parameter in the text. The references in this figure are Boore et al. (1997), Sadigh et al. (1997), Abrahamson and Silva (1997), Campbell et al. (2003), Spudich et al. (1999), Wells and Coppersmith (1994), Ellsworth (WG02), and Hanks and Bakun (2002).

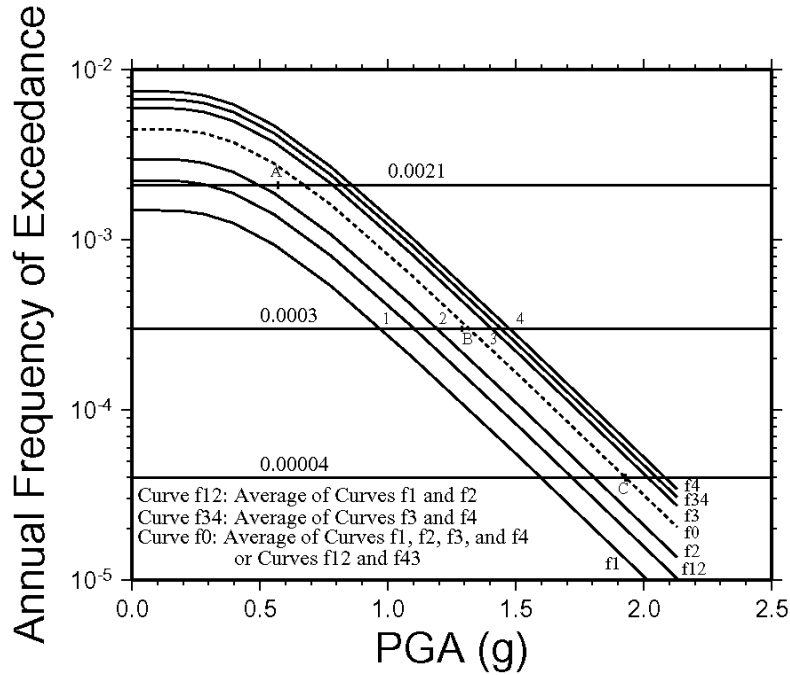


Figure 2. A schematic figure to show the hazard curves from Monte Carlo sampling and the mean hazard curve. This figure explains how the common approach calculates the mean ground motion values and the uncertainties. It averages the ground motion values (marked by 1, 2, 3, and 4 for risk value 0.0003) from each hazard curve and may leave some of the sampled hazard curves uncounted. For example, curve f1 is not counted for risk value 0.0021. Therefore, the mean ground motion values vary in the sensitivity analysis. The approach used in this study calculates the mean hazard curve (f0, obtained by averaging the AFE) and the AFE uncertainty first and then calculates the ground motion uncertainty. The symbols “A”, “B”, and “C” mark the average ground motion values at three risk values from common approach.

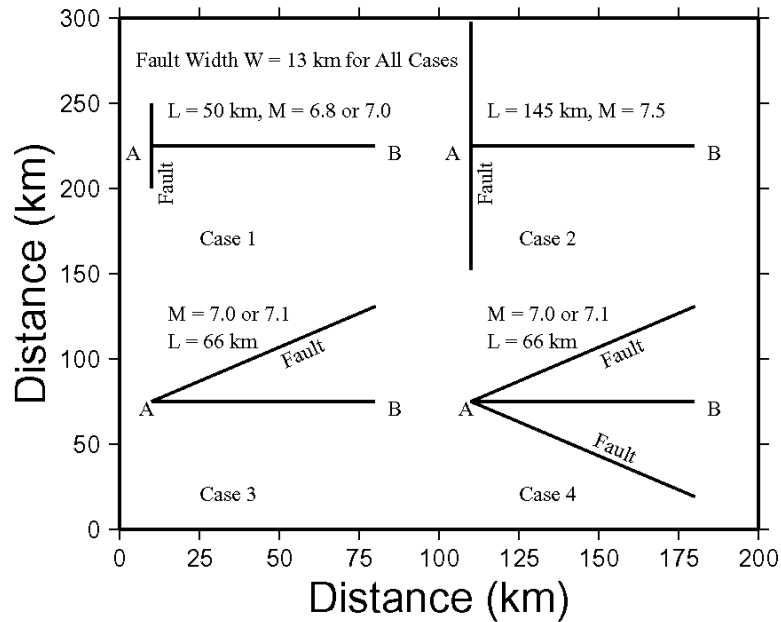


Figure 3. A schematic figure to show the fault geometry for the four test cases. Assuming class B fault in all cases. The fault slip rate is 5 ± 2 mm/year for all the cases. The angle between the fault and line AB is 58 degrees in Case 3. It looks small than that because the scales are different in vertical and horizontal axes. The angle between two faults in Case 4 is twice of 58 degrees. The magnitudes in cases 1, 2, and 4 are from different area-magnitude relations (see text for details).

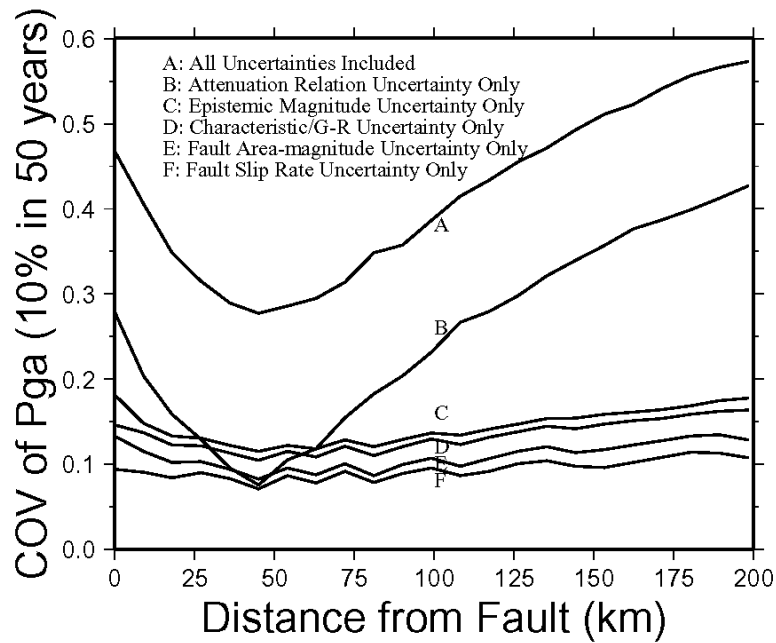


Figure 4. The COV of ground motion (10% of exceedance in 50 years) as a function of distance for all model uncertainties and for one by one model element uncertainties (sensitivity). This figure is for test Case 1 with moderate fault magnitudes ($M \sim 7.0$). The total uncertainty is dominated by the attenuation relation uncertainty, which has strong distance dependence.

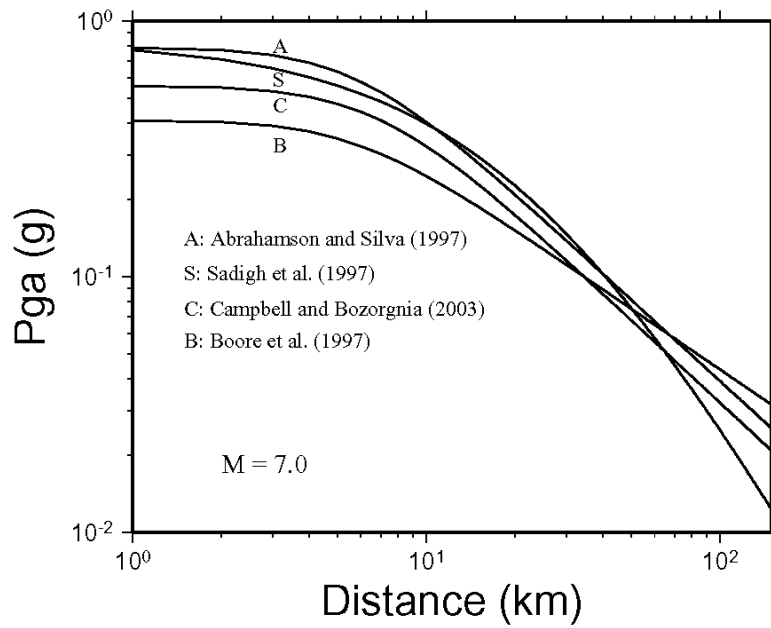


Figure 5. The four attenuation relations used in the 2002 update of California hazard model (Fig. 1). The strong distance dependence of uncertainties shown in Figure 4 due to the attenuation relations is obviously due to better data constraint to all relations around distance 40 to 50 km and less constraint at near and far distances.

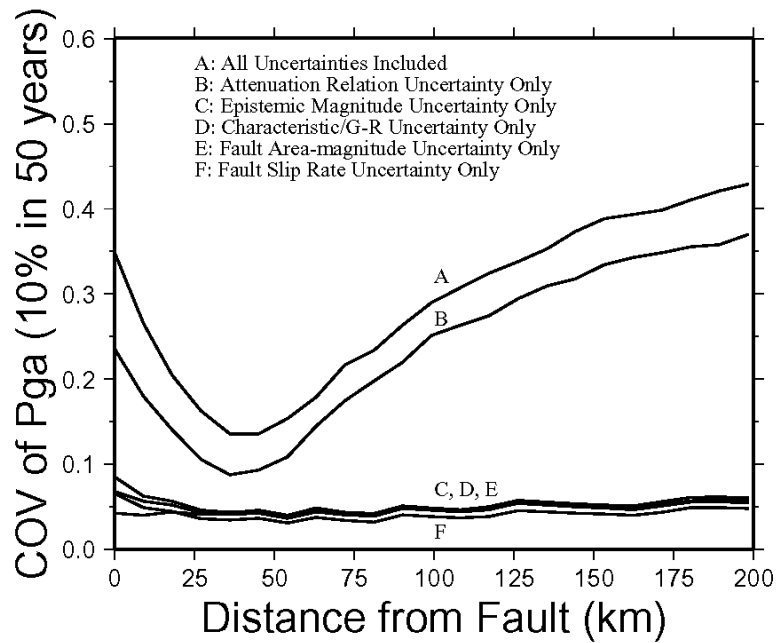


Figure 6. The COV of ground motion as a function of distance. It is for test Case 1 but with 2% of exceedance in 50 years. The total uncertainty as well as the uncertainty for each model element decrease compared to Figure 4 (10% in 50 years). The uncertainty due to attenuation relations decreases the least.

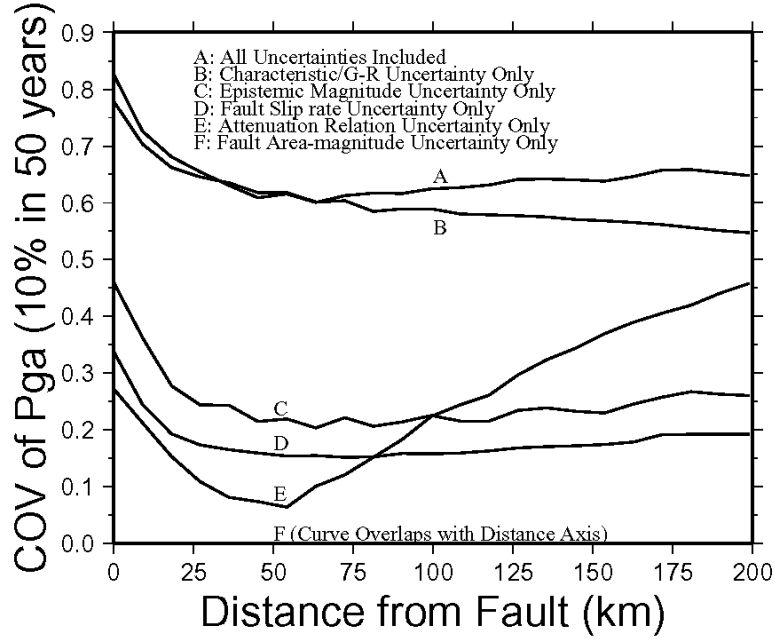


Figure 7. The COV of ground motion (10% of exceedance in 50 years) as a function of distance for test Case 2 with a large fault magnitude ($M \sim 7.5$). The uncertainty due to the characteristic vs. G-R modeling increases the most and becomes dominant. The pattern that the COV values decrease with distance from the fault and then increase for faults with moderate magnitudes ($M \sim 7.0$) is now changed to decreasing with distance from the fault and then leveling off. The uncertainties due to epistemic magnitude uncertainty and fault slip uncertainty also increase.

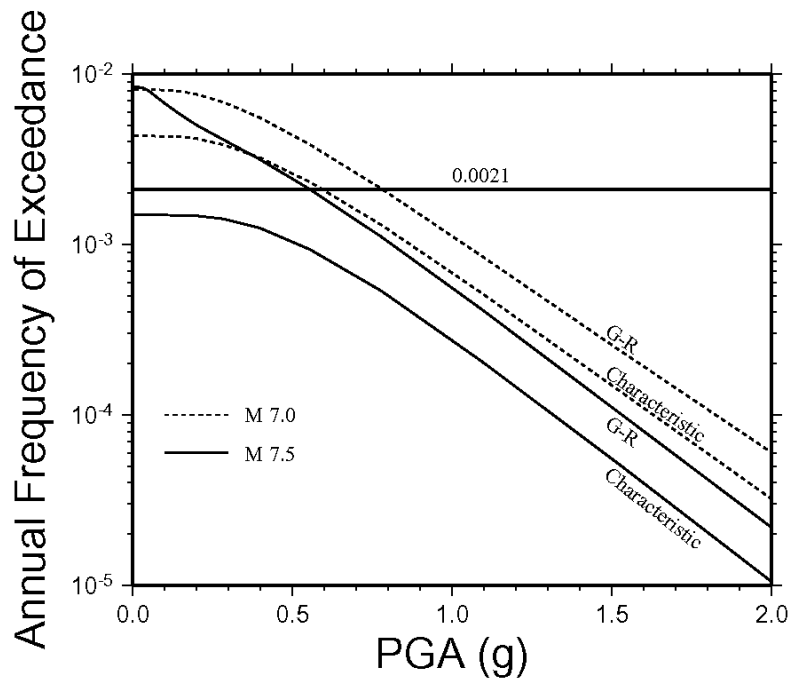


Figure 8. The hazard curves of site A in test Cases 1 and 2 when the characteristic vs. G-R modeling is the only uncertainty considered. The difference of ground motion values between characteristic model and G-R model is much larger for the large magnitude than for the moderate magnitude at a risk value of 0.0021. The differences between characteristic model and G-R model decrease for both magnitudes at lower risk values.

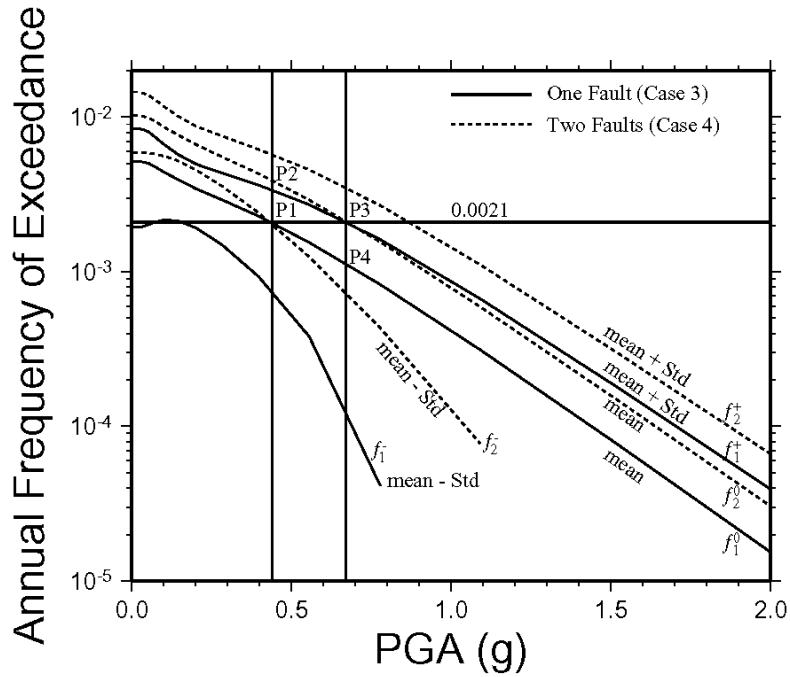


Figure 9. The mean hazard curves (f_1^0 and f_2^0) and the mean plus and minus one STD curves (f_1^+ , f_1^- , f_2^+ , and f_2^-) at site A in test Cases 3 and 4. P1 and P3 are the cross points of curves f_1^0 and f_2^0 with the line for a risk value 0.0021. P2 is the cross point of f_2^0 with the vertical line going through point P1; P4 is the cross point of f_1^0 with the vertical line going through P3. The following relations are shown in the text: (1) the AFE of f_2^0 is twice of f_1^0 at any given PGA for both independent and dependent samplings; (2) the COV of AFE at P2 is the same as at P1 if dependent sampling is used and 30% lower if independent sampling is used (the statistical effect); (3) the same relation of (2) exists between points P3 and P4; (4) the COV of AFE at P4 is lower than at P1 because of the lower risk value or higher PGA value at P4 (the hazard effect); (5) the same relation of (4) exists between P2 and P3; and (6) the COV of AFE at P3 is much lower than at P1 due to both effects.

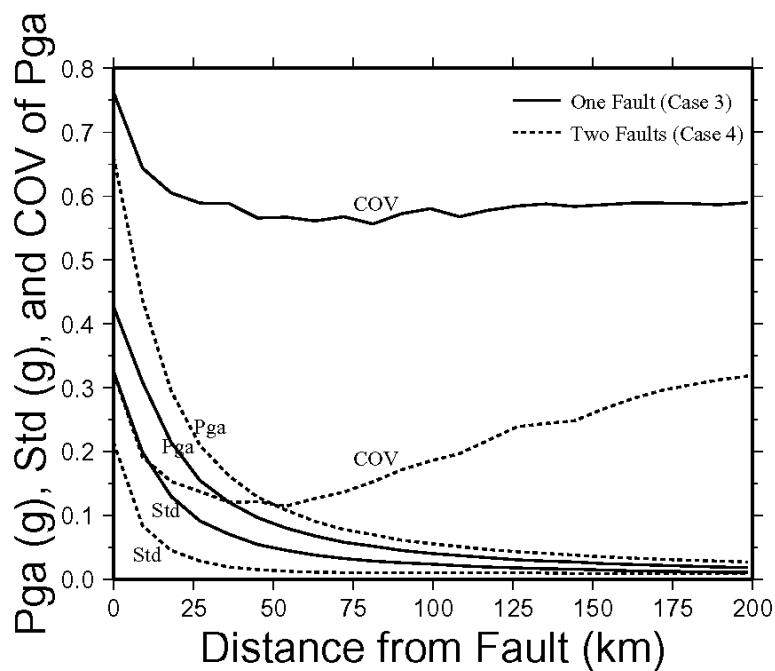


Figure 10. The COV of PGA curves from test Cases 3 and 4 at site A with independent sampling. The PGA values increase from a one-fault to a two-fault system. But it is not like AFE values that are exactly doubled from a one-fault to a two-fault system. Both the COV and STD of PGA decrease significantly from a one-fault to a two-fault system due to the statistical and hazard effects.

Fault Map

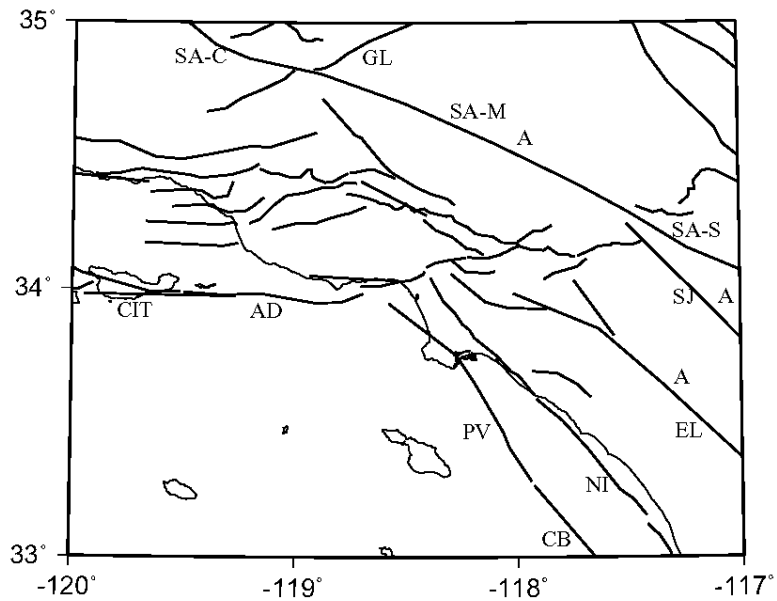


Figure 11. The fault map for the tri-county region. The class A faults are labeled with “A”. The abbreviations are “SA-M” for Mojave segment of San Andreas fault, “SA-C” for Carrizo segment, “SA-S” for San Bernardino segment, “GL” for Garlock fault, “SJ” for San Jacinto fault, “EL” for Elsinore fault, “NI” for Newport-Inglewood fault, “CB” for Coronado Bank fault, “PV” for Palos Verdes fault, “AD” for Anacapa-Dume fault, and “CIT” for Channel Islands Thrust fault.

All Uncertainties Included

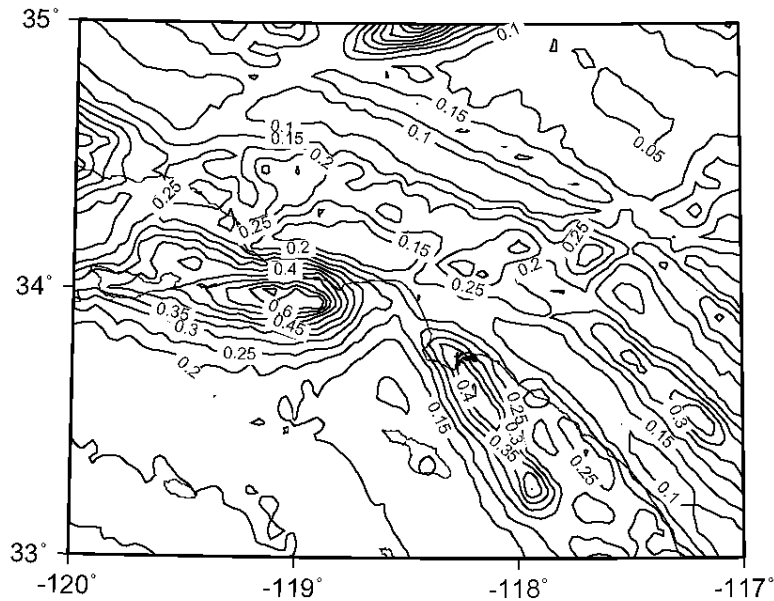
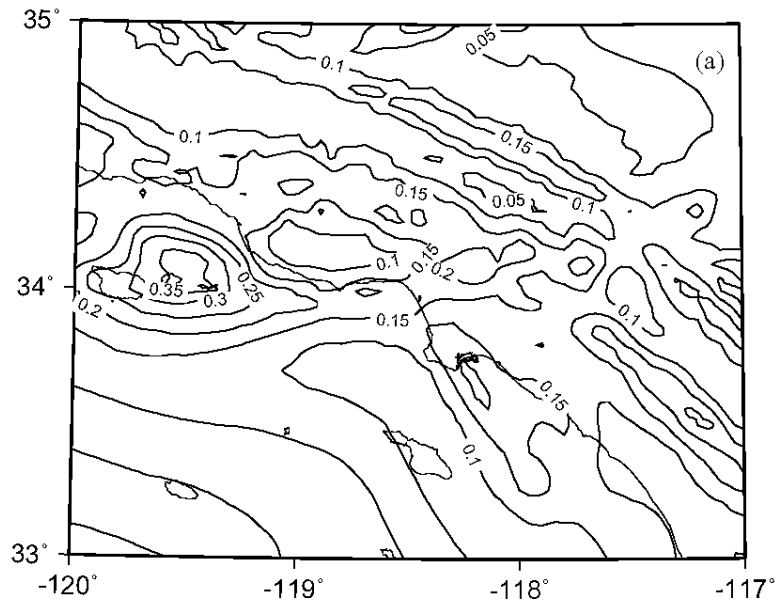
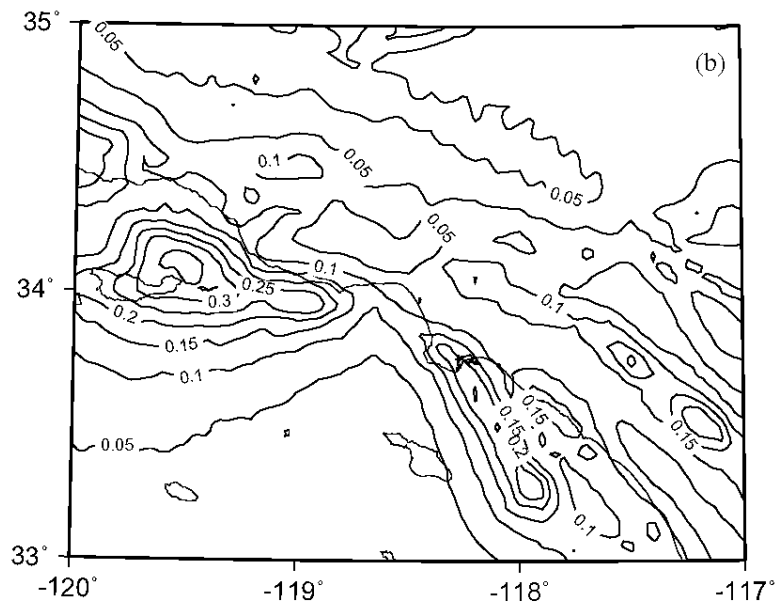


Figure 12. The COV of PGA (10% in 50 years) map for the tri-county region with all the model uncertainties included except the uncertainties from background seismicity. The COV values are about 0.1 to 0.15 along class A faults and about 0.2 to 0.3 along most of the B faults. The high COV values (0.4 to 0.6) are around the Garlock, Anacapa-Dume, and Palos Verdes faults. The contours make U-turns at both ends of the Mojave segment, where more than one fault or one segment are close to each other. These are typical samples for the statistical and hazard effects and can be found at many other places on this map.

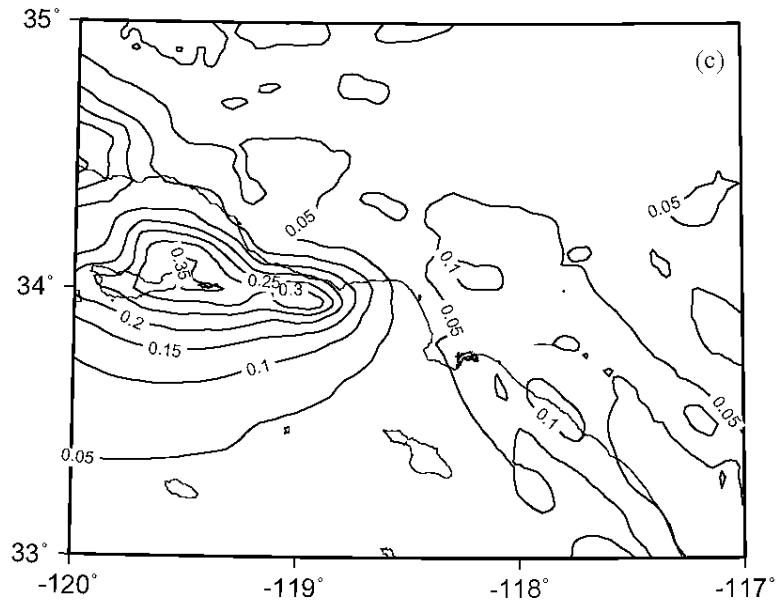
Attenuation Uncertainty Only



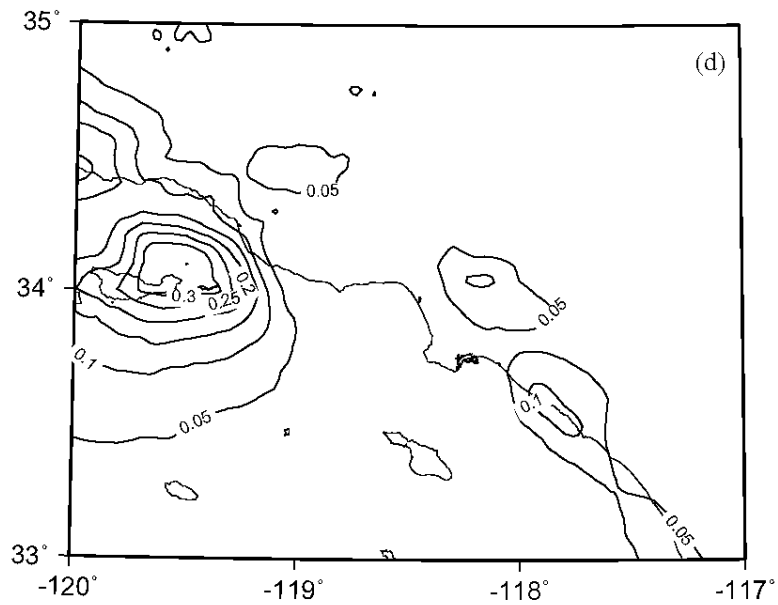
Magnitude Uncertainty Only



Slip Rate Uncertainty Only



Area-magnitude Uncertainty Only



Characteristic/G-R Uncertainty Only

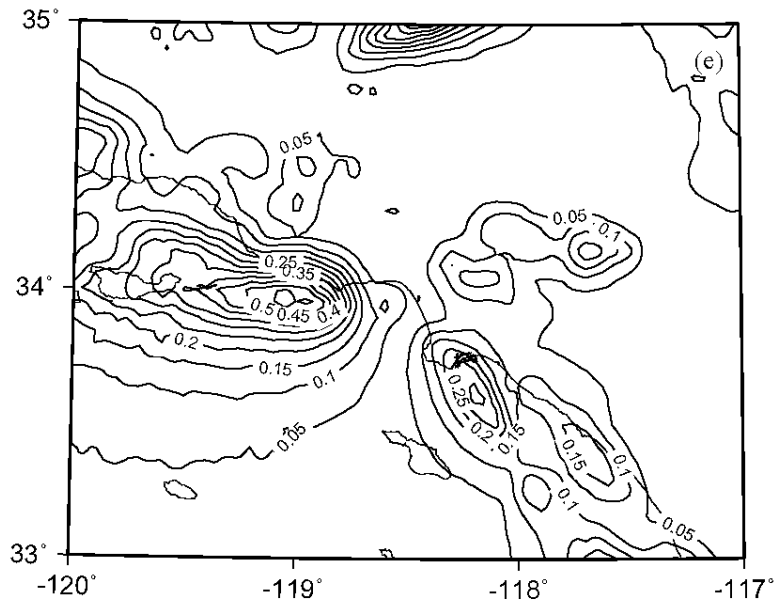


Figure 13. The five COV of PGA maps for showing the sensitivity analysis results with (a) for attenuation uncertainty only, (b) for epistemic magnitude uncertainty only, (c) slip rate uncertainty only, (d) for area-magnitude uncertainty only, and (e) for characteristic v . G-R modeling only. The attenuation and epistemic magnitude uncertainties are the two leading contributors for most of the area. At the area of poorly defined faults like Anacapa-Dume fault, the attenuation, epistemic magnitude, fault slip rate, and characteristic v . G-R modeling all contribute high uncertainties, especially the characteristic v . G-R modeling.

B-G Seismicity Uncertainty Only

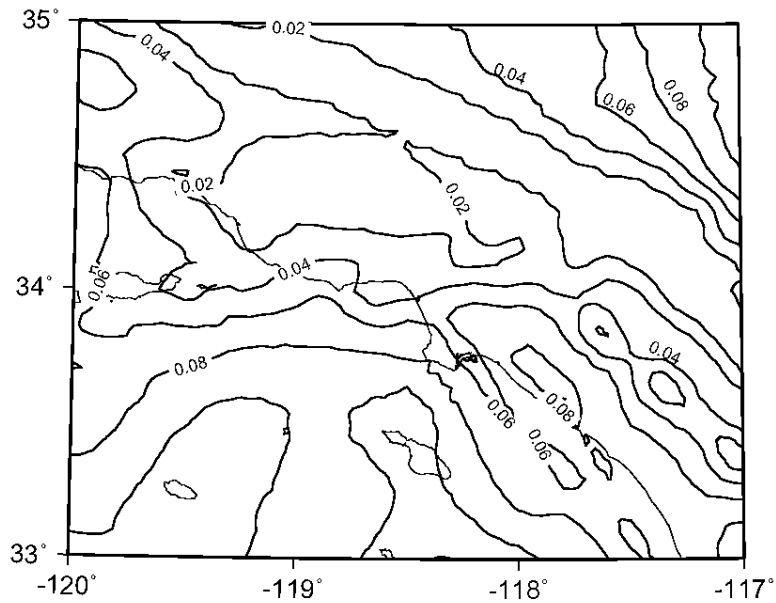


Figure 14. The COV of PGA (10% in 50 years) map for the uncertainties from background seismicity only. This map is produced with the total mean hazards of fault and background sources. In Figures 12 and 13 the background hazards are not included. The uncertainty contribution from background seismicity is very low compared with the fault sources. It is interesting to note that the contours are still showing the distribution of fault traces but in a reversed way that the uncertainties are the lowest along the faults. It is exactly showing that the uncertainties from background seismicity are due to the seismicity off the faults.

Fault Map

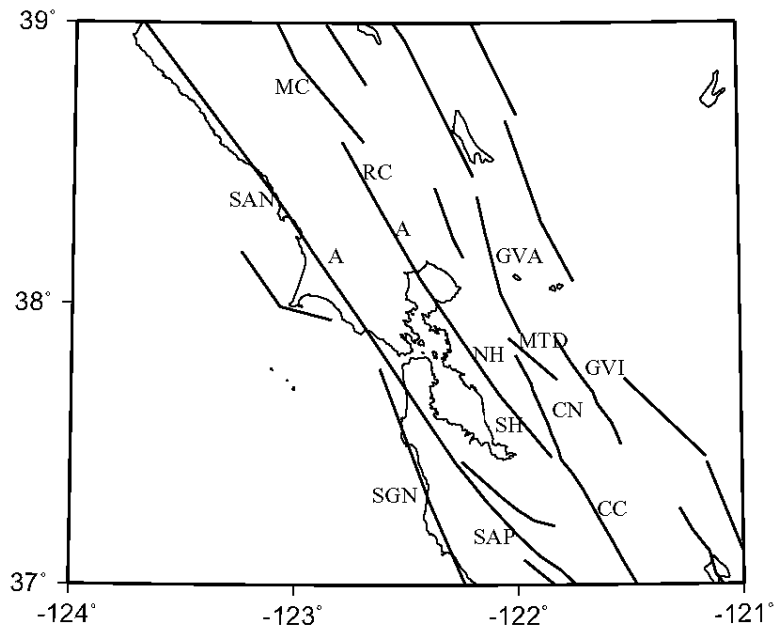


Figure 15. The fault map for the San Francisco Bay region. The class A faults are labeled with symbol "A". The abbreviations for the fault names are "SAN" for San Andreas North Coast, "SAP" for San Andreas Peninsula, "SGN" for San Gregorio North, "CC" for Calaveras Central, "CN" for Calaveras North, "SH" for Hayward South, "NH" for Hayward North, "RC" for Rodgers Creek, "MC" for Maacama, "GVA" for Green Valley, "GVI" for Greenville, and "MTD" for Mt. Diablo.

All Uncertainties Included

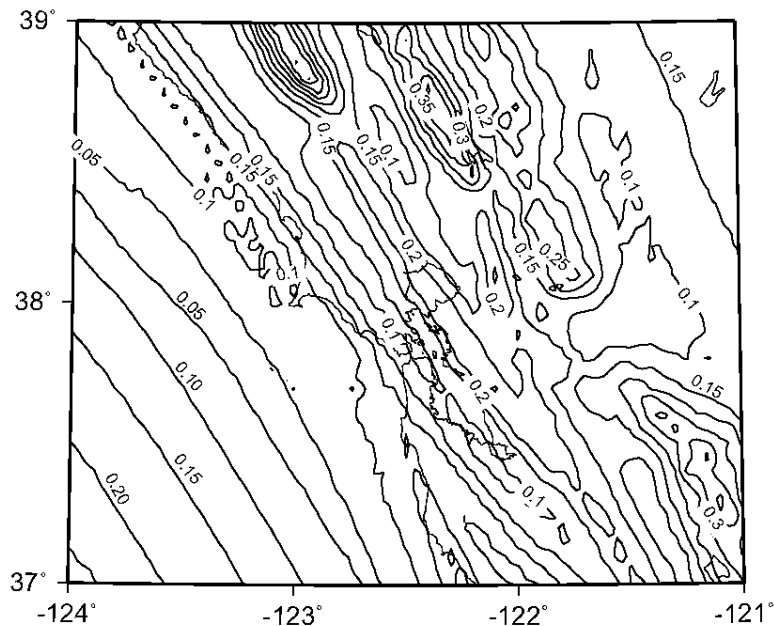


Figure 16. The COV of PGA (10% in 50 years) map for the San Francisco Bay region with all the model uncertainties included except the uncertainty from background seismicity. The COV values along the class A fault and those class B faults but studied in the WG02 are around 0.1 to 0.15 similar to the tri-county region. It is 0.2 to 0.3 along the class B faults in the southeast and north parts of the region, which are not studied by WG02. The pattern of COV decreasing with distance from the fault and then increasing (Case 1) is very clear in the west from the San Andreas fault far into the ocean. There are no sources to interrupt this pattern in the west direction. This pattern is overwhelmed by local sources and background seismicity in the east direction. The decrease of COV due to statistical and hazard effects can be found in many localized areas like between Maacama and Rodgers Creek faults and among many faults around the Mt. Diablo Fault area.

**COV of Peak Acceleration (g)
with 10% Probability of Exceedance in 50 Years**

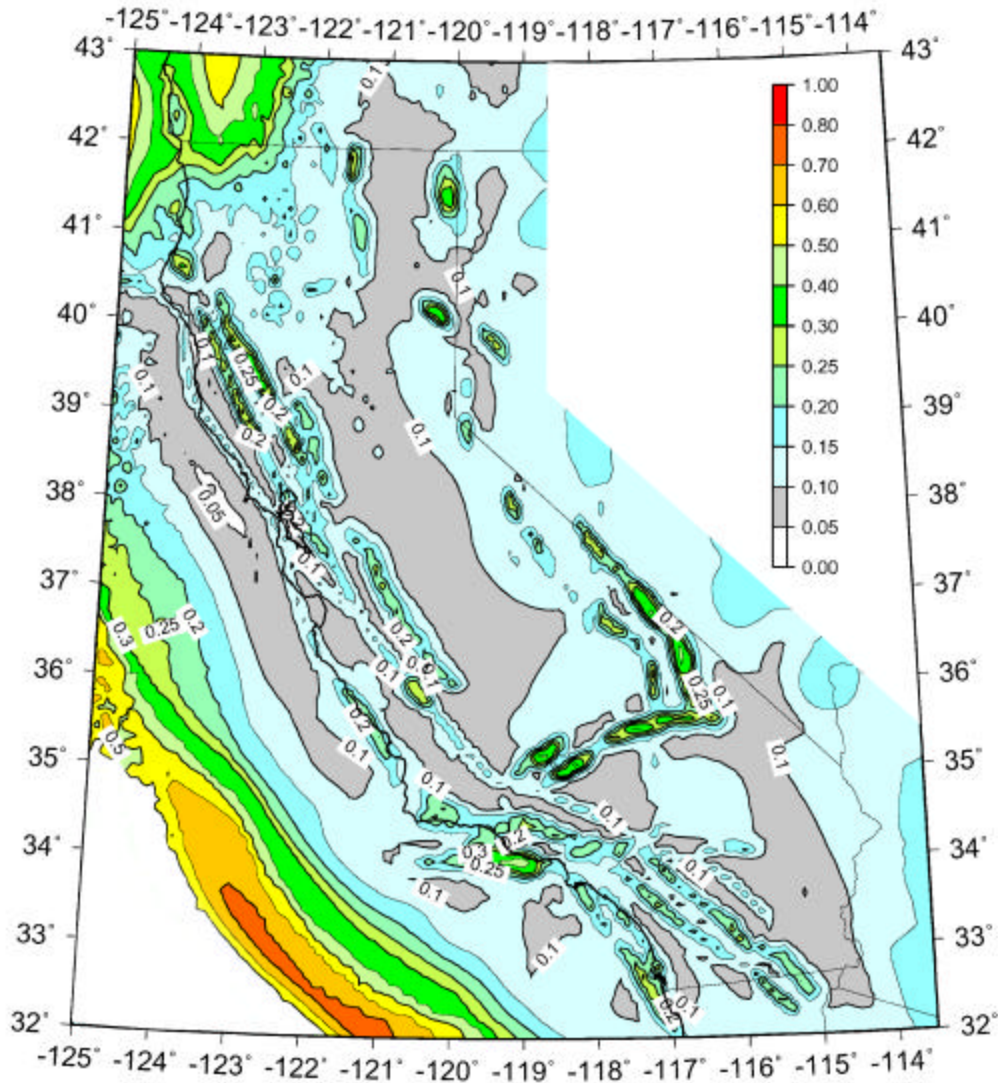


Figure 17. The COV of PGA (10% in 50 years) map for California. The COV values along the San Andreas fault system from southern to northern California are about 0.1 to 0.15. It decreases with distance from fault in both directions east and west and then increases. The COV values along most of the class B faults are 0.2 to 0.3. The pattern that COV increases at large distances from fault is not overwhelmed by local sources to the west into the ocean but is overwhelmed in central and east California by the local and Nevada sources and the background seismicity. The high COV values are observed around Anacapa-Dume, Palos Verdes, and Garlock faults in southern California and around Maacama fault and Cascadia subduction zone in northern California. These are poorly defined faults with large magnitudes.

